Supplementary Information

Discontinuous Coordination Boosting Ion Transport in Solid Polymer Electrolytes

Bochun Liang,[a,b,‡] Xue-Yan Huang,[c,‡] Shendong Tan,[a] Tairan Wang,[b] Chaoyuan Ji,[a] Ting Si,[b] Xi-Yao Li,[c] Hao Chen,[a,d] Yaoshu Xie,[a] Lu Jiang,[e] Chen-Zi Zhao,*[c] Jun Fan,*[b] Tingzheng Hou,*[a] and Qiang Zhang[c,f]

[a] Institute of Materials Research, Tsinghua Shenzhen International Graduate School, Tsinghua University, Shenzhen, 518055, P. R. China.

[b] Department of Materials Science and Engineering, City University of Hong Kong, Hong Kong, 999077, P. R. China

[c] Beijing Key Laboratory of Complex Solid State Batteries & Tsinghua Center for Green Chemical Engineering Electrification, Department of Chemical Engineering, Tsinghua University, Beijing, 100084, P. R. China

[d] Department of Chemistry, University of Chinese Academy of Sciences, Beijing 100049, P. R. China

[e] Department of Materials Science and Engineering, City University of Hong Kong (Dongguan), Dongguan, 523808, P. R. China

[f] The Innovation Center for Smart Solid State Batteries, Yibin 644002, P. R. China

‡ These authors contributed equally to this work.

Note 1. Experiments

Electrochemical Measurements

Electrochemical measurements were carried out on an electrochemical station (Solartron EnergyLab XM). The ionic conductivity of the solid-state electrolytes was measured by electrochemical impedance spectroscopy (EIS) with a frequency from 1 MHz to 0.1 Hz at the amplitude of 10 mV. A corresponding cell was assembled using two polished stainless-steel blocking electrodes in an Ar-filled glove box (O_2 < 0.1 ppm, H_2O < 0.1 ppm). The ionic conductivity σ was calculated from the following equation:

$$\sigma = \frac{d}{S \times R_b} \quad (1)$$

where d (cm) is the thickness of the solid-state membrane, S (cm^2) is the area of the stainless-steel electrode, and R_b (Ω) is the bulk resistance of the electrolyte membrane measured by EIS. The Li^+ transference number (t_+) of the solid-state polymer electrolyte was measured by a chronoamperometry test on a Li|polymer electrolyte|Li cell with an applied voltage of 10 mV. Based on the measured values, t_+ was calculated by following equation:

$$t_+ = \frac{I_S(\Delta V - I_0 R_0)}{I_0(\Delta V - I_S R_S)} \quad (2)$$

where ΔV (V) is the potential applied across the cell, and the initial (I_0) and steady-state (I_s) currents are obtained from the chronoamperometric curve. R_0 and R_s measured by EIS reflect the initial and steady-state resistances of the passivating layers.

Linear sweep voltammetry (LSV) measurements were performed using Li foils as both

reference and counter electrodes, and carbon-coated Al foils as the working electrode. The potential was scanned positively from 2.0 V to 6.0 V *vs.* Li^+/Li at a rate of 0.5 mV s^{-1} on a Solartron 1470E electrochemical workstation.

Cell Assembly and Measurements

For the $LiFePO_4$ (LFP) cathode, the cathode slurry was fabricated by mixing 80 wt.% LFP, 10wt.% Super P, and 10 wt.% polyvinylidene difluoride (PVDF, Alfa Aesar) in N-methyl-2-pyrrolidone (NMP, Aldrich) solution. The cathodes were obtained by coating the slurry onto aluminium foil by knife coater and dried in a vacuum oven at 80°C for over 12 h. The loading of LFP was around 5 mg cm^{-2}. The foils were cut into circular cathodes with a diameter of 10 mm. The 2025 coin-typed solid-state cell was assembled by placed the cathode in the positive shell firstly, 100 μL polymer/LiTFSI (Li^+:Oe = 1:20) solution mixture was added into cathode at 80 °C, then polyethylene separator was placed. 100 μL polymer/LiTFSI solution mixture was added into separator. The cathode and separator with solution mixture were vacuumized and dried at 80 °C in order to infiltrate the cathode and remove the solvent. Second, the lithium anode, spacer, and battery spring were placed in turn, then the negative shell was finally covered. All cells were assembled in an argon-filled glovebox with O_2 and H_2O contents below 0.1 ppm. A LAND multichannel battery testing system (Wuhan LAND Electronics Co., Ltd.) was used to perform electrochemical measurements. The charge-discharge voltage range was 3.0–3.8 V for LFP cathodes. The

1 C rate was determined to be 170 mA g^{-1} in LFP cell testing. Critical current density (CCD) was measured using Li/polymer electrolyte/Li symmetric cells and evaluated using a stepwise current increment protocol: each charge/discharge cycle was conducted for 1 h, starting at 0.1 mA cm^{-2} with 0.1 mA cm^{-2} increments between steps.

Materials Characterizations

^{1}H nuclear magnetic resonance (NMR) experiments for pure polymers were performed using a JEOL JNM-ECZ400S, $CDCl_3$ (PTHF, PEO and PDOL) and $(CD_3)_2SO$ (PTOM) as solvent at room temperature. ^{7}Li solid-state MAS NMR experiments was performed on a JEOL JNM-ECZ600R spectrometer, and the samples were packed into the center of the tubes (diameter=3.2mm) and the spinning rates were set to 12 kHz. Differential scanning calorimetry (DSC) of the polymer electrolyte materials was recorded on a NETZSCH DSC-200PC instrument from 80℃ to −90℃ and −90℃ to 80℃. The structures of the electrolytes and polymers were characterized with *in situ* attenuated total reflection Fourier transform infrared spectrograph (ATR-FTIR, NICOLET 6700).

Note 2. Simulation Procedures

Classical molecular dynamics simulations

The generation of polymer chain topologies and the force field assignment were done with the assistance of the mBuild[1] and foyer[2] package. After this, the initial polymer chain for simulations was prepared by an energy minimization process and a relaxation process using only Van der Wals interaction with a distance cut-off of 6 Å for a few hundred picoseconds. The as-prepared chain was then duplicated to random distribution using a python script and mixed with Li^+ and $TFSI^-$ in the simulation box using the Moltemplate program.[3] Before the MD simulation, the simulation box was treated with a soft potential to un-overlap atoms. Components in simulation boxes for these electrolyte systems are listed in Table S1. The simulation box is shown in Fig. S1. The setups were chosen by benchmarking the ionic conductivity with box sizes. Details are shown in Fig. S2 and Table S2.

For simulations of the glass transition, details will be discussed in Supplementary Note 3. For normal simulations, each system was first equilibrated using a conjugate gradient energy minimization, followed by an annealing process of 40 ns in the NPT ensemble at 1 bar (heating from 100 K to 800 K for 10 ns, cooling from 800 K to the target temperature for 20 ns, and another 10 ns maintaining the target temperature). After this, the system was equilibrated in the NVT ensemble for 230 ns with the last 200 ns for analysis. For each system, three independent simulations were conducted with different initial structures.

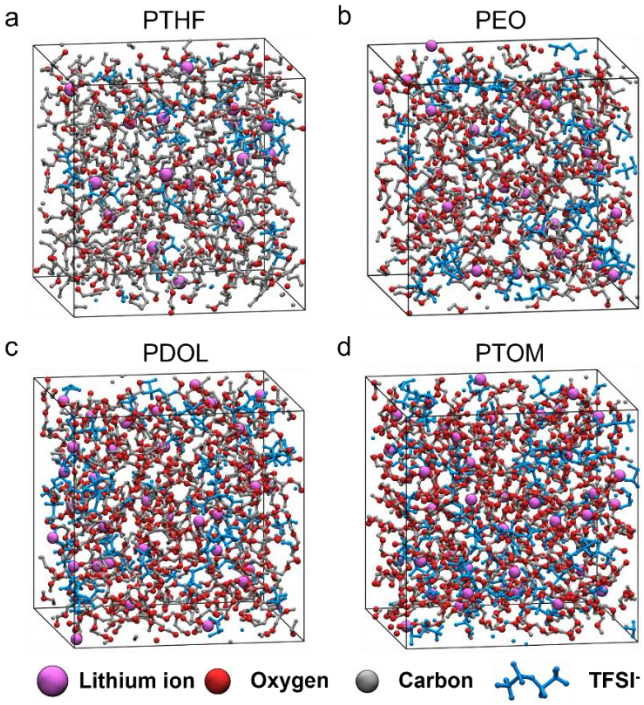

Fig. S1. MD Simulations box for (a) PTHF, (b) PEO, (c) PDOL, and (d) PTOM.

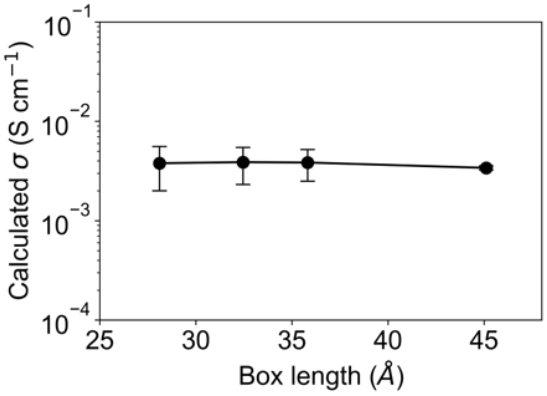

Fig. S2. Convergence test of ionic conductivity *vs.* box length for MD simulations.

Ab initio molecular dynamics

Limited by the scales of *Ab initio* molecular dynamics (AIMD) simulation, relatively short chains were adopted to mimic the polymer chain. Components in each simulation box

are listed in Table S3. Each system was first optimized using the LBFGS algorithm,[4] followed by an NPT relaxation at 423 K and 1 atm for 30~40 ps to obtain a reasonable box size. The box size evolutions with simulation time in NPT simulations are shown in Fig. S4. The initial structure for the final NVT run was obtained by averaging the box sizes over 10 ps after convergence during the NPT run, and then getting the cell with the most similar box size with the average box size from the NPT trajectory. After this, the system was relaxed in NVT ensemble at 423 K for 60 ps using the velocity rescaling CSRV thermostat.[5] The last 50 ps NVT run was used for analysis.

The association lifetime of Li^+–Oe τ_s was obtained from the continuous time correlation function:[6]

$$S(t) = \frac{\langle H(t)h(0)\rangle}{\langle h(0)\rangle} \quad (3)$$

where $h(t) = 1$ if Oe is in the first solvation shell of Li^+ and 0 otherwise. $H(t) = 1$ if Oe is in the first solvation shell of Li^+ at $t = 0$ and remains continuously up to time t, and 0 otherwise. The coordination states were determined by the radial distribution function $g(r)$ (Fig. S5), from which Li–Oe cut-off distances were chosen: 2.6 Å for PTHF, 3.0 Å for PEO, 3.0 Å for PDOL, and 2.6 Å for PTOM. The calculated *S(t)* results are shown in Fig. S6. τ_s was calculated by doing a biexponential fit on *S(t)* as done in the reference.[7]

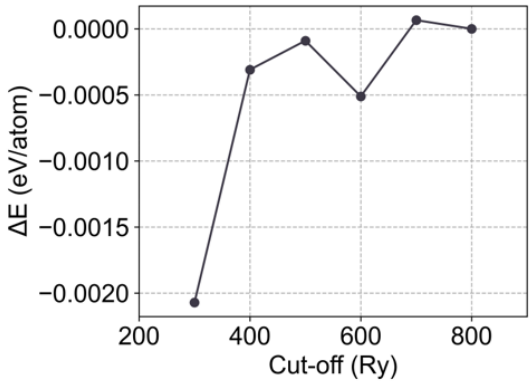

Fig. S3. Convergence test for plane wave cut-off. ΔE is calculated as the difference between total energy with a specific plane wave cut-off and that with a plane wave cut-off of 800 Ry.

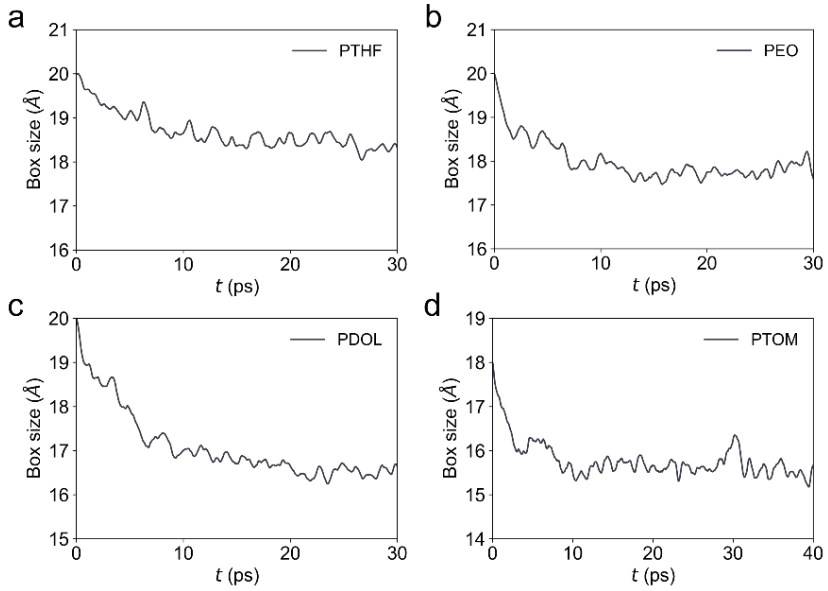

Fig. S4. Box size evolution with simulation time in NPT simulations for (a) PTHF, (b) PEO, (c) PDOL, and (d) PTOM.

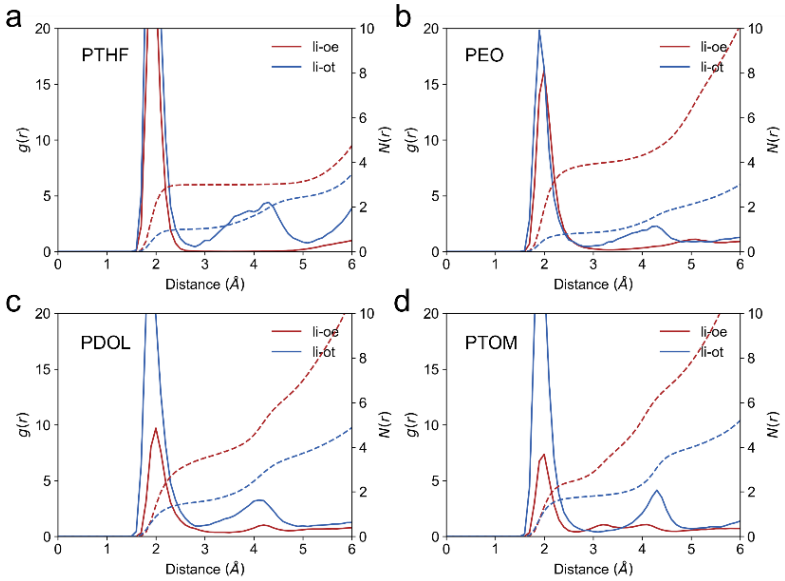

Fig. S5. Coordination analysis from AIMD simulations for (a) PTHF, (b) PEO, (c) PDOL, and (d) PTOM.

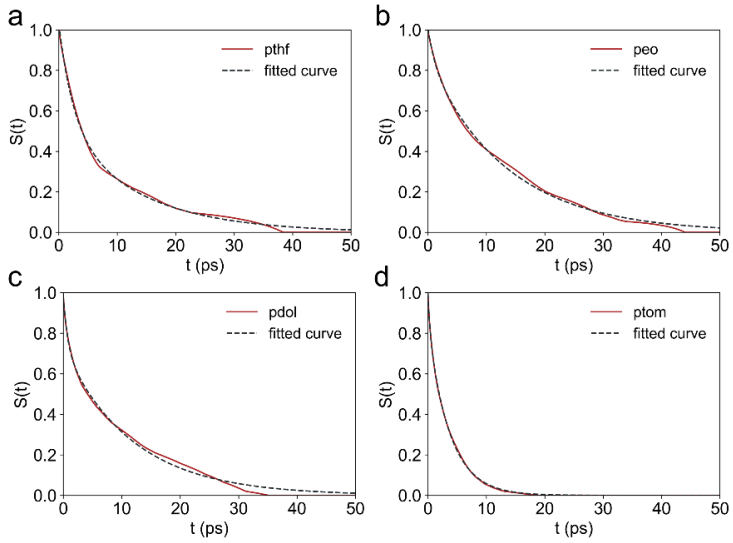

Fig. S6. The continuous time correlation function and the biexponential fit for (a) PTHF, (b) PEO, (c) PDOL, and (d) PTOM.

Note 3. Transport Properties

The self-diffusion coefficient (D), ionic conductivity (σ), and lithium transference numbers (t_+) were obtained from MD simulation. To be specific, D was calculated using the Eistein relation from the mean-square displacement of the molecule center of mass or target particles:

$$\mathrm{MSD}(t) = \frac{1}{N}\sum_i^N < [\boldsymbol{r}_i(t_0 + t) - \boldsymbol{r}_i(t_0)]^2 > \quad (4)$$

$$D = \lim_{t\to\infty} \frac{\mathrm{MSD}(t)}{6t} \quad (5)$$

where $[\boldsymbol{r}_i(t_0 + t) - \boldsymbol{r}_i(t_0)]$ is the displacement of particle i during time t over a possible starting time t_0 within the studied trajectory, and < > denotes the ensemble average. D was calculated by obtaining the slope of MSD over the linear region (diffusive regime) larger than 5 ns. MSDs of Li^+ and $TFSI^-$ for representative systems are presented in Fig. S7.

The prediction of σ and t_+ mainly relies on the Onsager framework[8] for electrolyte transport integrating continuum mechanics, nonequilibrium thermodynamics, and electromagnetism, which gives rise to Onsager transport coefficients that quantify ion correlations in an electrolyte, provided solid approaches to calculate the ionic conductivity and cation transference number in liquid electrolytes[9, 10] and polymer electrolytes[11-13] based on MD simulations. To be specific, the Onsager transport coefficients can be calculated using Green-Kubo relations:

$$L^{ij} = \frac{1}{6k_BTV}\lim_{t\to\infty}\frac{d}{dt}\langle\sum_\alpha[r_i^\alpha(t) - r_i^\alpha(0)]\cdot\sum_\beta\left[r_j^\beta(t) - r_j^\beta(0)\right]\rangle \quad (6)$$

where V is the volume and k_BT is the thermal energy, r_i^α is the position of particle α

relative to the center-of mass position of the entire system. The fraction of specific correlation is calculated by:

$$P(L^{ij}) = \frac{L^{ij}}{\sum_i \sum_j L^{ij}} \tag{7}$$

The ionic conductivity can be obtained by:

$$\sigma = F^2 \sum_i \sum_j L^{ij} z_i z_j \tag{8}$$

or in the Green-Kubo form:

$$\sigma = \frac{1}{6k_B TV} \lim_{t\to\infty} \frac{d}{dt} \langle \sum_i z_i [r_i^{\alpha}(t) - r_i^{\alpha}(0)] \cdot \sum_j z_j [r_j^{\beta}(t) - r_j^{\beta}(0)] \rangle \tag{9}$$

where, F is Faraday's constant, z_i is the charge of species i. The collective MSDs for calculating σ of representative systems are presented in Fig. S8. The lithium transference number can be calculated by:

$$t_+ = \frac{\sum_j L^{ij} z_i z_j}{\sum_k \sum_l L^{kl} z_k z_l} = \frac{L^{++} z^+ z^+ + L^{+-} z^+ z^-}{L^{++} z^+ z^+ + 2L^{+-} z^+ z^- + L^{--} z^- z^-} \tag{10}$$

Transport properties calculations were performed by the MDGO package.[10]

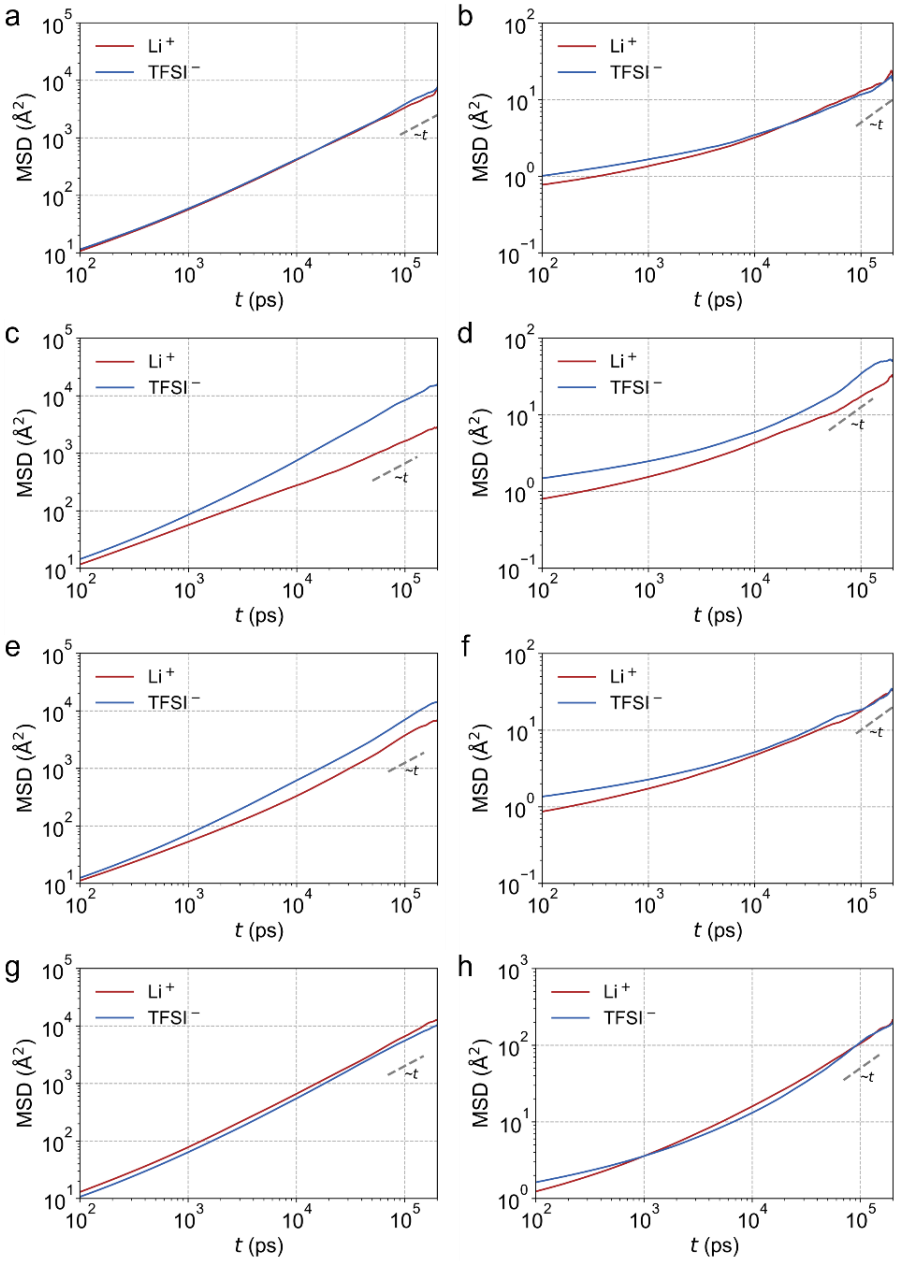

Fig. S7. Representative MSDs of Li^+ and $TFSI^-$ diffusion in PTHF at (a) 423 K and (b) 298 K, PEO at (c) 423 K and (d) 298 K, PDOL at (e) 423 K and (f) 298 K, and PTOM at (g) 423 K and (h) 298 K. The slope of the MSD on a log-log scale close to 1 indicates the diffusion regime.

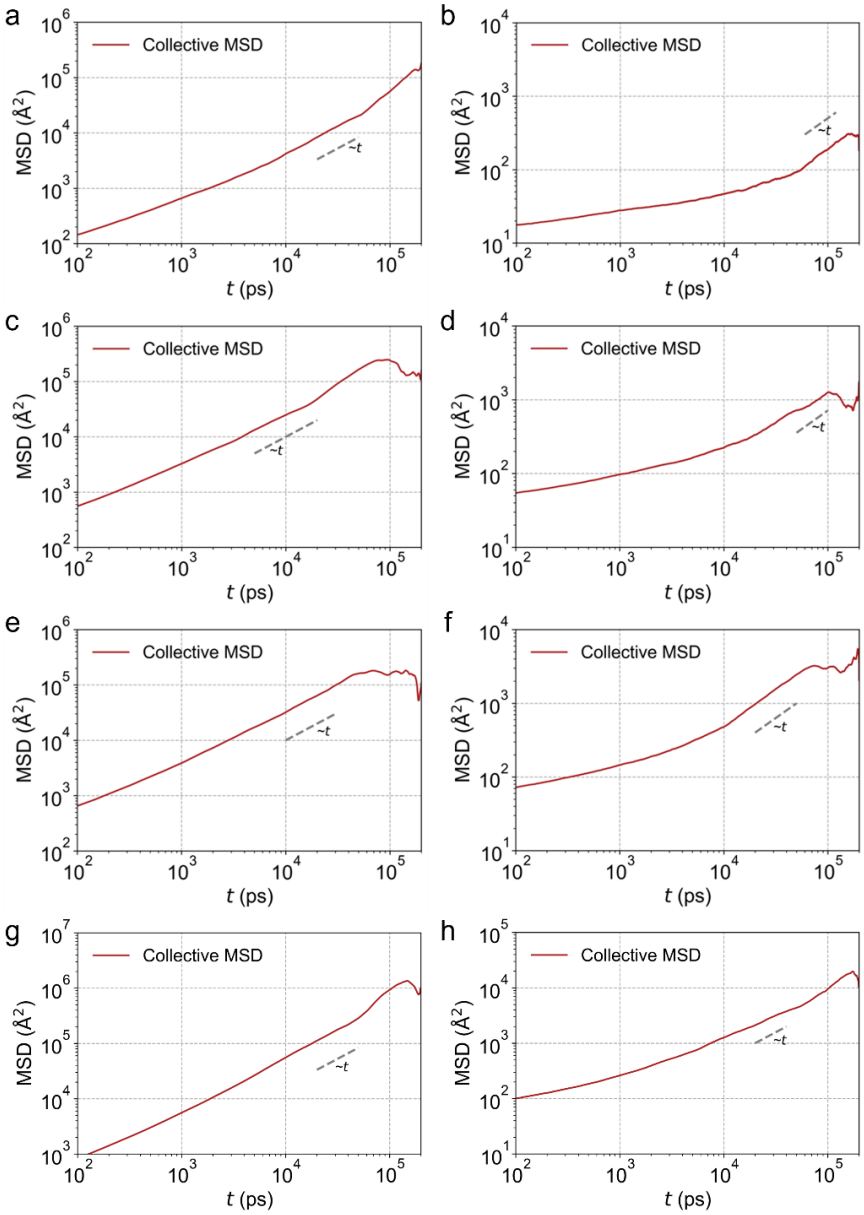

Fig. S8. Representative collectives MSDs of PTHF at (a) 423 K and (b) 298 K, PEO at (c) 423 K and (d) 298 K, PDOL at (e) 423 K and (f) 298 K, and PTOM at (g) 423 K and (h) 298 K. The slope of the collective MSD on a log-log scale close to 1 indicates the diffusion regime.

Note 4. Glass Transition Temperature

The glass transition temperature (T_g) was determined by the equation of state (PVT relationship)[14,15] using MD simulations. To obtain the V–T curve, each system was firstly annealed to a high temperature in an NPT ensemble at 1 bar (heated from 100 K to 800 K for 10 ns, cooled from 800 K to 500 K for 20 ns, and then equilibrated at 500 K for another 20 ns). Then, the equilibrated system was cooled continuously from 500 K to 20 K with a cooling rate of 1 K/ns at 1 bar in an NPT ensemble. For every cooling dT of 20 K (20 ns), the system was equilibrated for another 20 ns, and the specific volume was obtained by the average of the equilibrated specific volume during this period. The obtained V–T curves are shown in Fig. S9. Two regions distinguished by the slope can be found in each curve, namely the glassy state and the rubbery state.

Then, T_g was determined as the intersection of the extrapolated linear fit lines of the two regions. Since the calculated T_g is sensitive to the fitting range, we did the linear fitting in different ranges to obtain a series of intersection and obtain the average as the final calculated T_g. Specifically, take PTHF as an example, we set a fixed start point (20 K for the glassy region and 440 K for the rubbery region) and regulate the end point in a range (100 K to 180 K for glassy state and 360 K to 280 K for rubbery state, with an interval of 20 K). Hence total 5 intercepts were obtained and averaged to get the calculated T_g. The error bar in Manuscript Fig. 1g shows the standard deviation of these values. The representative fitting curves for these systems and the corresponding fitting region are

shown in Fig. S9.

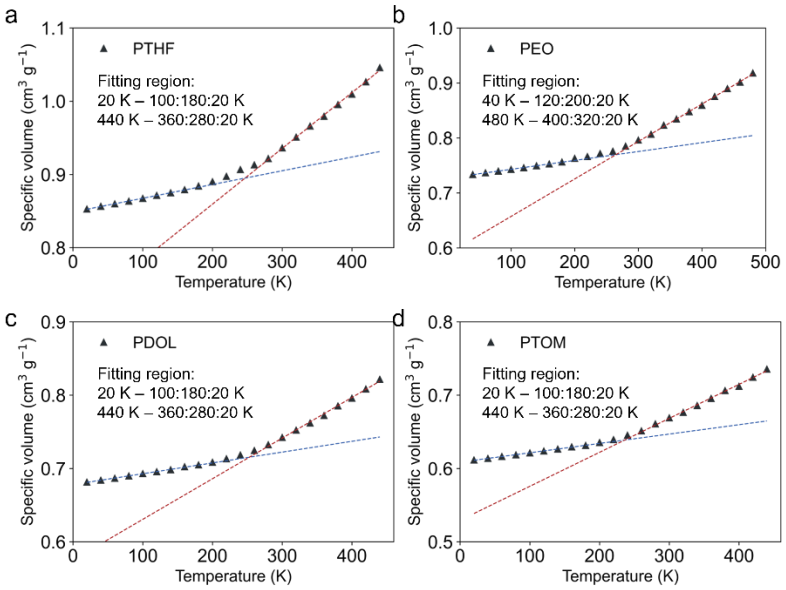

Fig. S9. The V–T curves for (a) PTHF, (b) PEO, (c) PDOL, and (d) PTOM. The dashed lines are the representative linear fits to obtain the intersections. The embedded text illustrates the fitting region for the glassy state and rubbery state.

Note 5. Coordination and Clustering Analysis

The coordination states were identified by the radial distribution function *g(r)* and the average number of the target atoms within radius of Li^+ *N(r)* (Fig. S10). An atom is considered in the first solvation shell or coordinated to Li^+ if the distance of Li^+–atom is within the cutoff distance (3.0 for Li^+–O and 5.0 for Li^+–N). The salt dissociation was characterized by the ion clustering analysis based on the Li^+–N($TFSI^-$) coordination with the assistance of the NetworkX package.[16]

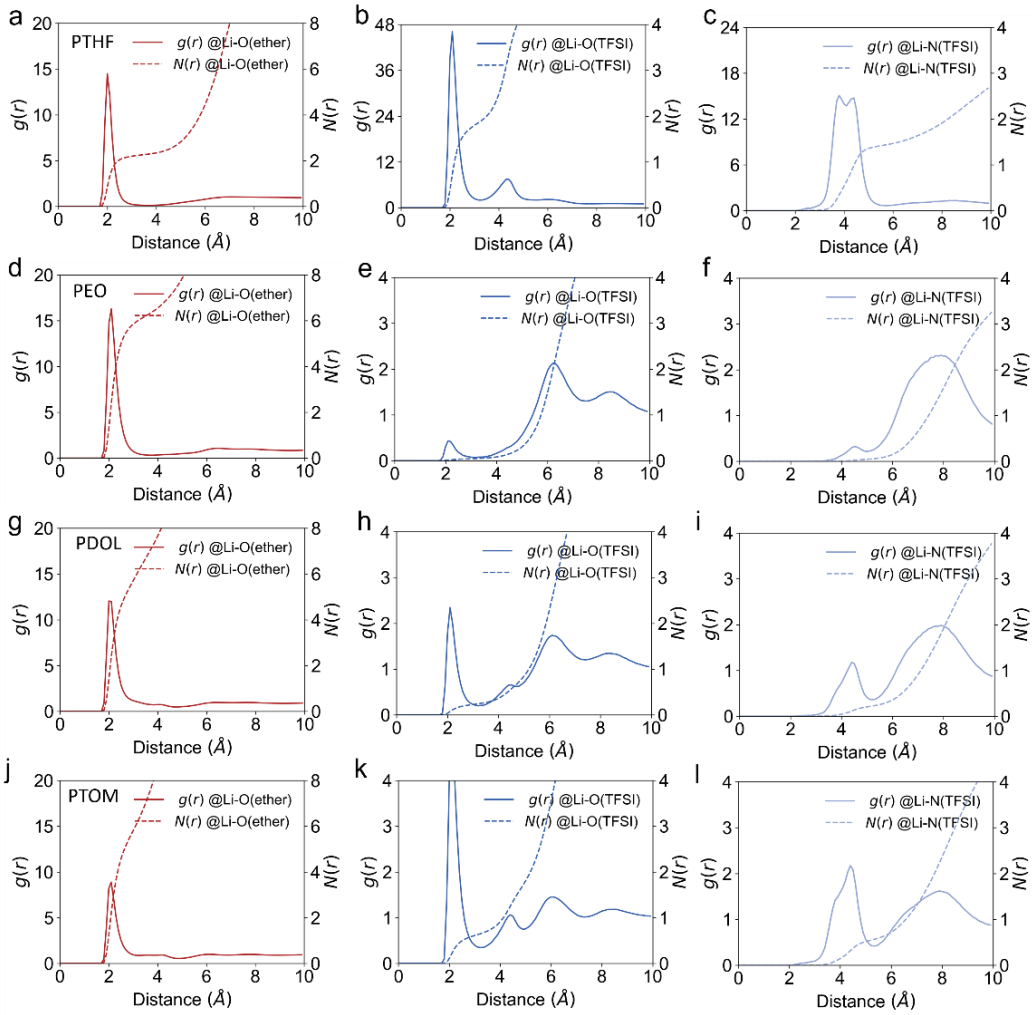

Fig. S10. The radial distribution function *g(r)* and the average number of the target atoms within radius of Li^+ *N(r)*. (a) Li^+–Oe, (b) Li^+–O($TFSI^-$), and (c) Li^+–N($TFSI^-$) for PTHF. (d) Li^+–Oe, (e) Li^+–O($TFSI^-$), and (f) Li^+–N($TFSI^-$) for PEO. (g) Li^+–Oe, (h) Li^+–O($TFSI^-$), and (i) Li^+–N($TFSI^-$) for PDOL. (j) Li^+–Oe, (k) Li^+–O($TFSI^-$), and (l) Li^+–N($TFSI^-$) for PTOM.

Note 6. Transport Modes Analysis

The Li^+ transport mechanisms were explored by analyzing the MD trajectory based on the approach developed by Heuer et al.[17] The basic information about the approach can be referred to in references [17-19]. We basically followed the definition of τ_1, τ_2, and τ_3 in these references except for the criteria of defining an intrachain or interchain event because of the difference in Li^+–polymer binding situations. This will be explained along with the introduction of the calculation method. To obtain τ_1, the Oe atoms were indexed continuously along polymer chains. The effective diffusion coefficient D_1 of Li^+ visit Oe along one or more polymer chains (one-dimension diffusion) is defined as

$$D_1 = \lim_{t\to\infty} \frac{\langle \Delta n^2(t) \rangle}{2t} \tag{11}$$

where $\Delta n(t)$ is the variance of the Oe atoms indices which are visited by a Li^+ during time interval t. Then τ_1 was obtained from the following definition:

$$\tau_1 = \frac{(N-1)^2}{\pi^2 D_1} \tag{12}$$

where N is the number of Oe atoms in one polymer chain (34 for PTHF, 54 for PEO, 68 for PDOL, and 81 for PTOM). As multiple-chain binding dominant was observed in some studied systems in the work, to enhance sampling, the criteria of intrachain hopping Li^+ being considered in the statistic is that the binding polymer chains of the observed Li^+ remains unchanged for at least 95% of the observation time t (as advised by reference [18]), no mater one-chain or multi-chain binding (different from references [17-19]). The representative $\langle \Delta n^2(t) \rangle$ for different systems is shown in Fig. S11. A slightly sub-

diffusive regime can be observed ($\langle \Delta n^2(t) \rangle \propto t^{0.8}$) for all systems, which is similar to previous reports.[18, 19] As statistic becomes worse at larger timescale, D_1 was directly estimated in the time range of τ_3 using $\frac{\langle \Delta n^2(\tau_3) \rangle}{2\tau_3}$.

The Rouse time τ_R of polymer chain that considering all Oe atoms was obtained by fitting the following relationship:

$$g(t) = \frac{2R_e^2}{\pi^2} \sum_{p=1}^{N-1} \frac{1-\exp\left(-\frac{p^2 t}{\tau_R}\right)}{p^2} \quad (13)$$

where $g(t)$ is the MSD of Oe atoms with respect to the center of mass of the corresponding polymer chain, R_e is the end-to-end distance of polymer chains, p denotes the mode number, and the sum is calculated over $(N-1)$ eigenmodes. The representative $g(t)$ is shown in Fig. S12. The calculated MSD $\sim t^{0.5}$ near the short time range and converges to the fitted $\frac{R_e^2}{3}$, indicating the well-captured Rouse-like behavior.[17] τ_2 was obtained using the same method as τ_R while considering only the Oe atoms bound to Li^+.

For interchain hopping, τ_3 was calculated by counting the number of interchain hopping events N_{inter} throughout the whole simulation time t_{sim} (200 ns):

$$\tau_3 = \frac{t_{\text{sim}} N_{\text{Li}}}{N_{\text{inter}}} \quad (14)$$

where N_{Li} is the number of Li^+ in the system. The criteria for counting an interchain hopping event is that the Li^+ binding polymer chains change (no matter one-chain binding or multi-chain binding) and the successive backjumps within 100 ps are excluded.

The obtained time scales and the structure properties of PEO were compared to those of

reference [19] under the same criteria where only one-chain binding was considered, as shown in Table S5. The reasonable agreement indicates the correctness of our code and the ability of the force field to predict the transport mechanism.

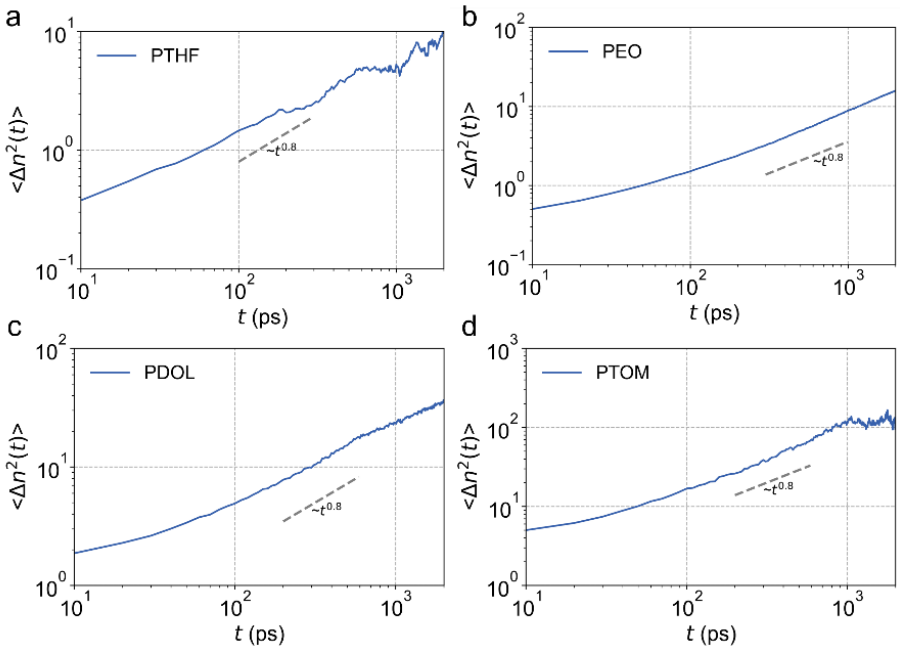

Fig. S11. Representative $\langle \Delta \boldsymbol{n^2(t)} \rangle$ of Li^+ diffuses along polymer chains for (a) PTHF, (b) PEO, (c) PDOL, and (d) PTOM. The slope of the $\langle \Delta \boldsymbol{n^2(t)} \rangle$ on a log-log scale close to 0.8 indicates the sub-diffusive behavior.

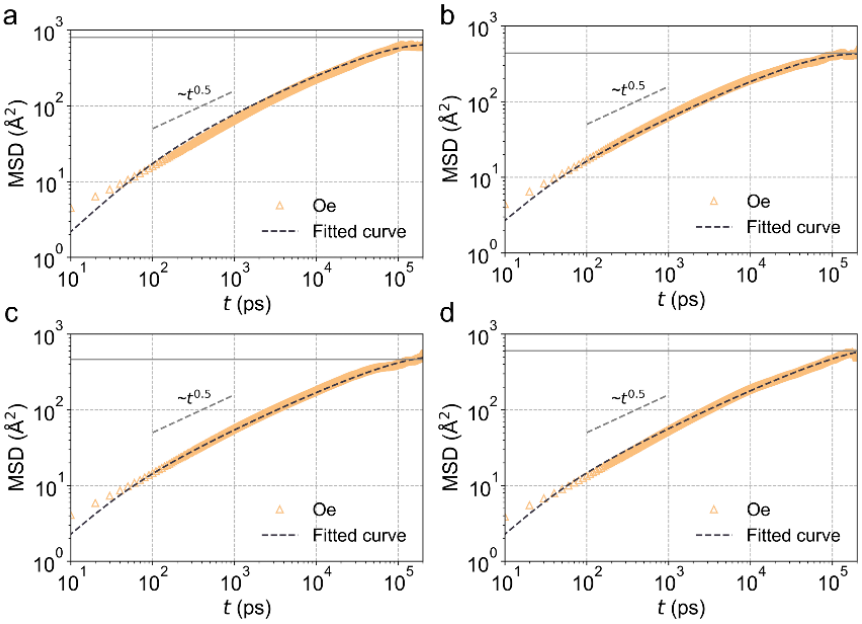

Fig. S12. Representative Oe MSDs with respect to the center of mass of the polymer chain for (a) PTHF, (b) PEO, (c) PDOL, and (d) PTOM. The Grey line stands for the fitted $\frac{R_e^2}{3}$. MSD ~ $t^{0.5}$ in the short time window indicates the Rouse-like behavior.[17]

Note 7. Results and Discussions

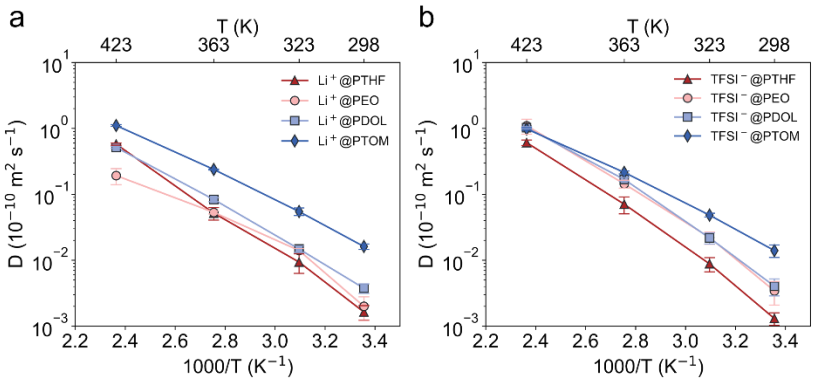

Fig. S13. The calculated self-diffusion coefficient of (a) Li^+ and (b) $TFSI^-$.

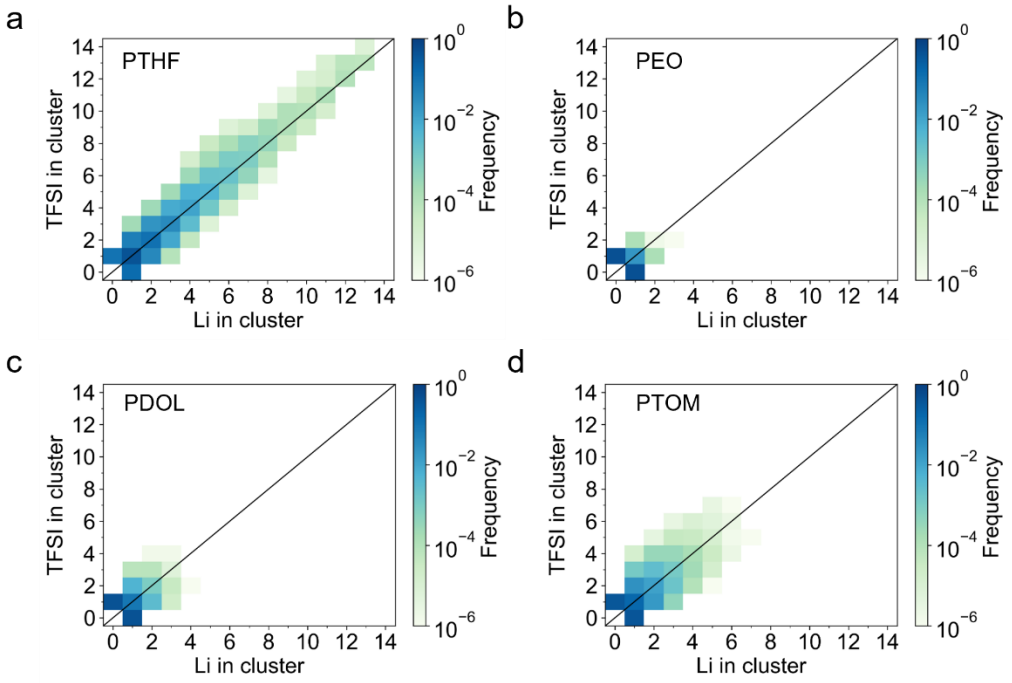

Fig. S14. Ion clustering statistics for (c) PTHF, (d) PEO, (e) PDOL, and (f) PTOM.

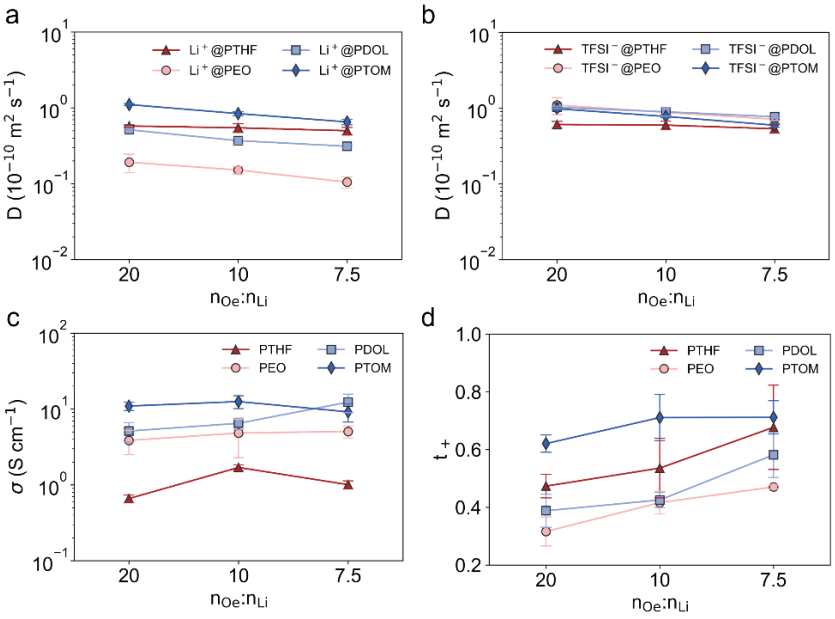

Fig. S15. Concentration effect on transport properties. The diffusion coefficient of (a) Li^+, and (b) $TFSI^-$, (c) the ionic conductivity σ, and (d) transference number t_+.

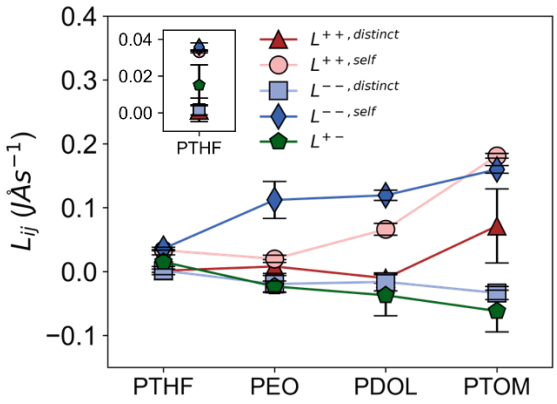

Fig. S16. Onsager transport coefficients L^{ij} for distinct cation–cation correlation, self-cation–cation correlation, distinct anion–anion correlation, self-anion–anion correlation, and cation–anion correlation.

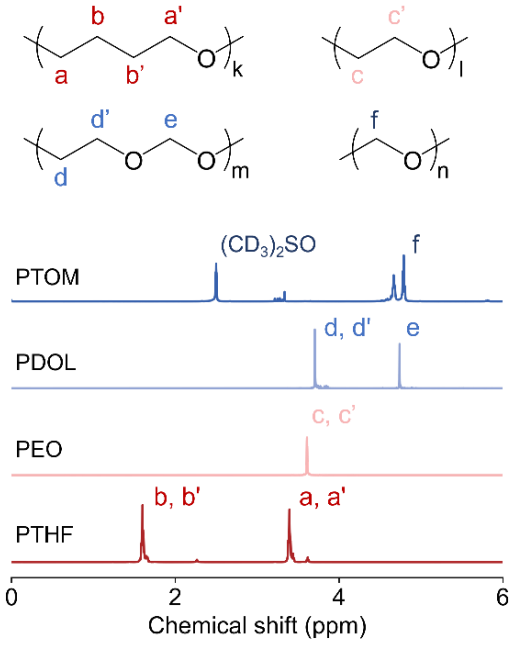

Fig. S17. ^{1}H NMR Spectra of the electrolytes.

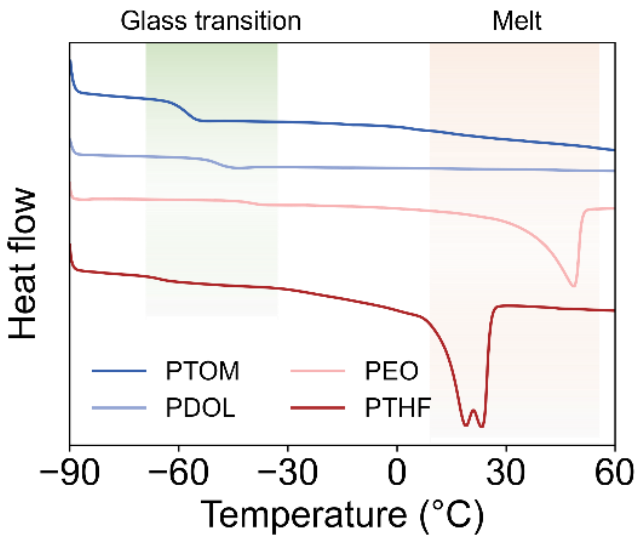

Fig. S18. DSC curves of the electrolytes.

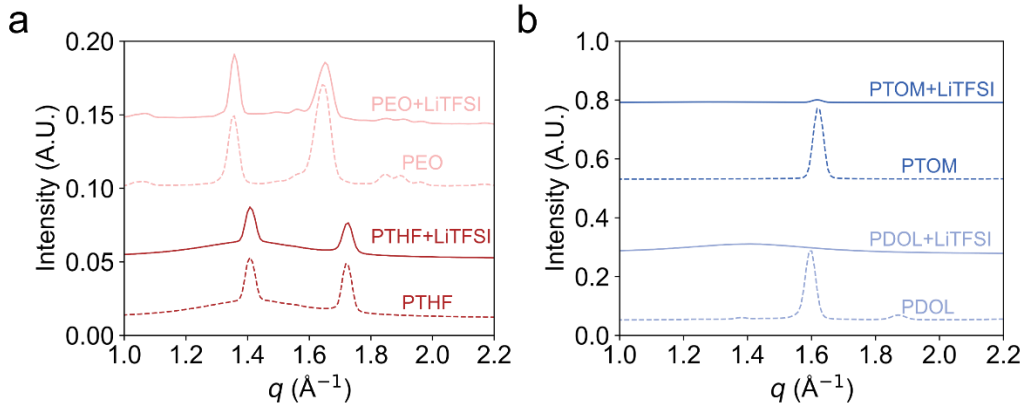

Fig. S19. Wide-angle X-ray scattering (WAXS) profiles for electrolytes and the corresponding pristine polymers.

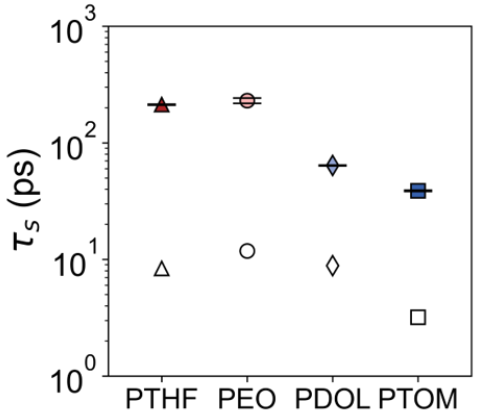

Fig. S20. The calculated Li–Oe association lifetime τ_s. The hollow labels are from AIMD simulation, and the filled labels are from MD simulations.

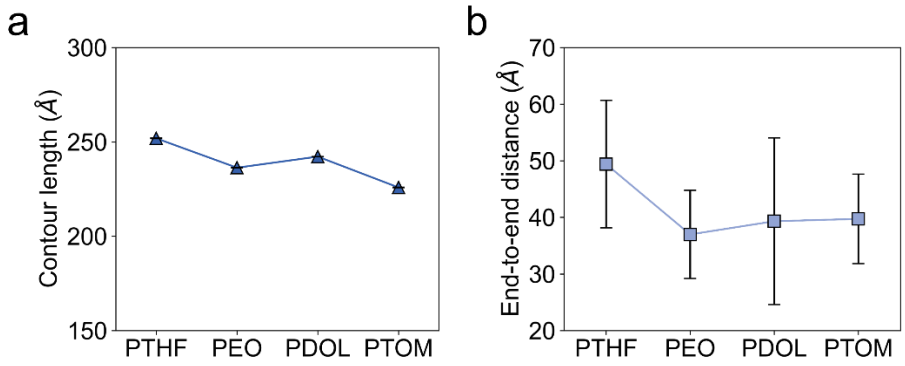

Fig. S21. Structure properties of the simulated polymers. (a) The contour length of polymer chains and (b) the end-to-end distance.

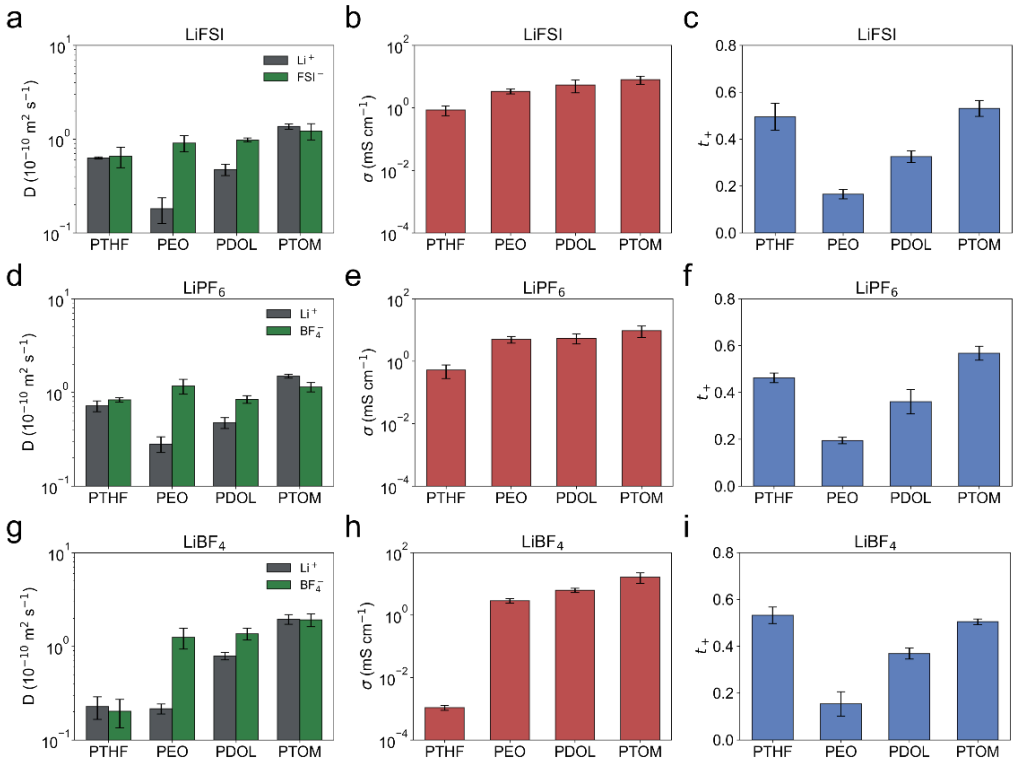

Fig. S22. The calculated diffusion coefficients of cation and anion, ionic conductivity, and Li^+ transference number in four polymers for (a)–(c) LiTFSI, (d)–(f) $LiPF_6$, and (g)–(i) $LiBF_4$.

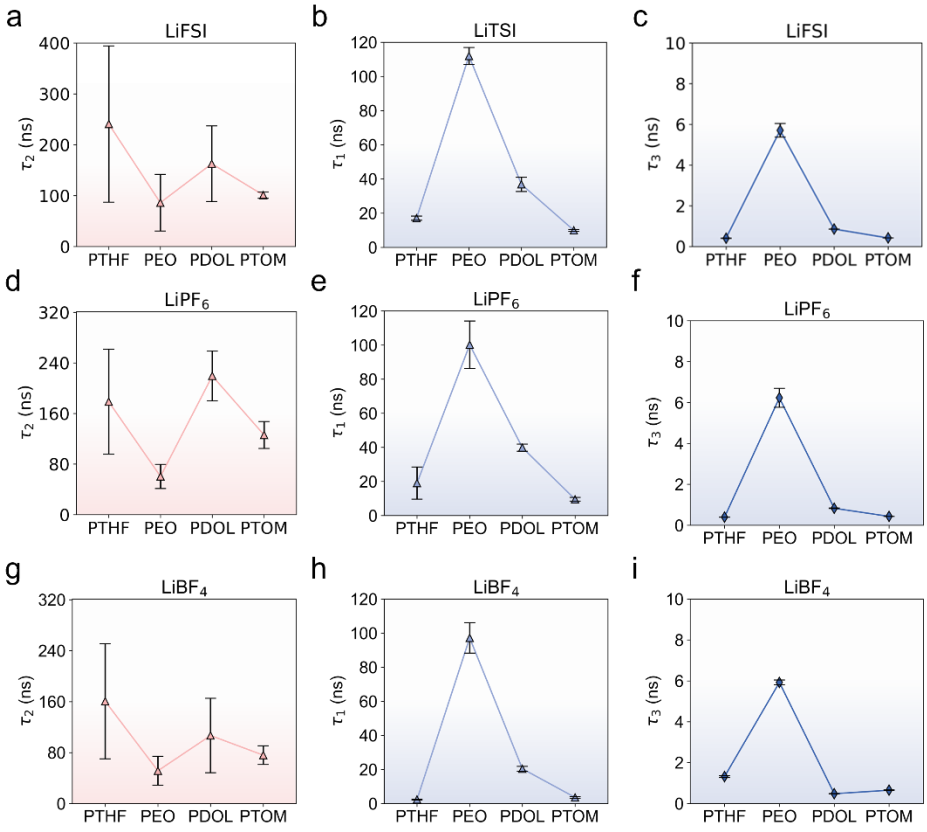

Fig. S23. The calculated characteristic timescales for Li^+ transport in four polymers for (a)–(c) LiTFSI, (d)–(f) $LiPF_6$, and (g)–(i) $LiBF_4$.

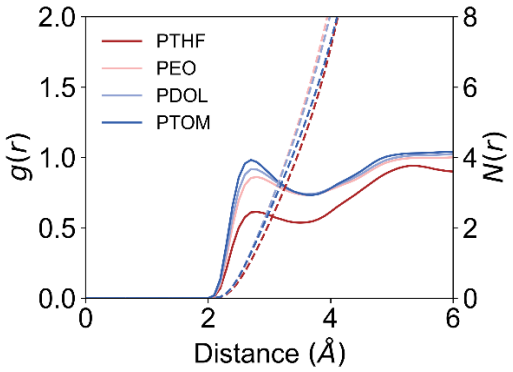

Fig. S24. The radial distribution function *g(r)* for O(TFSI$^-$)-H(polymer)

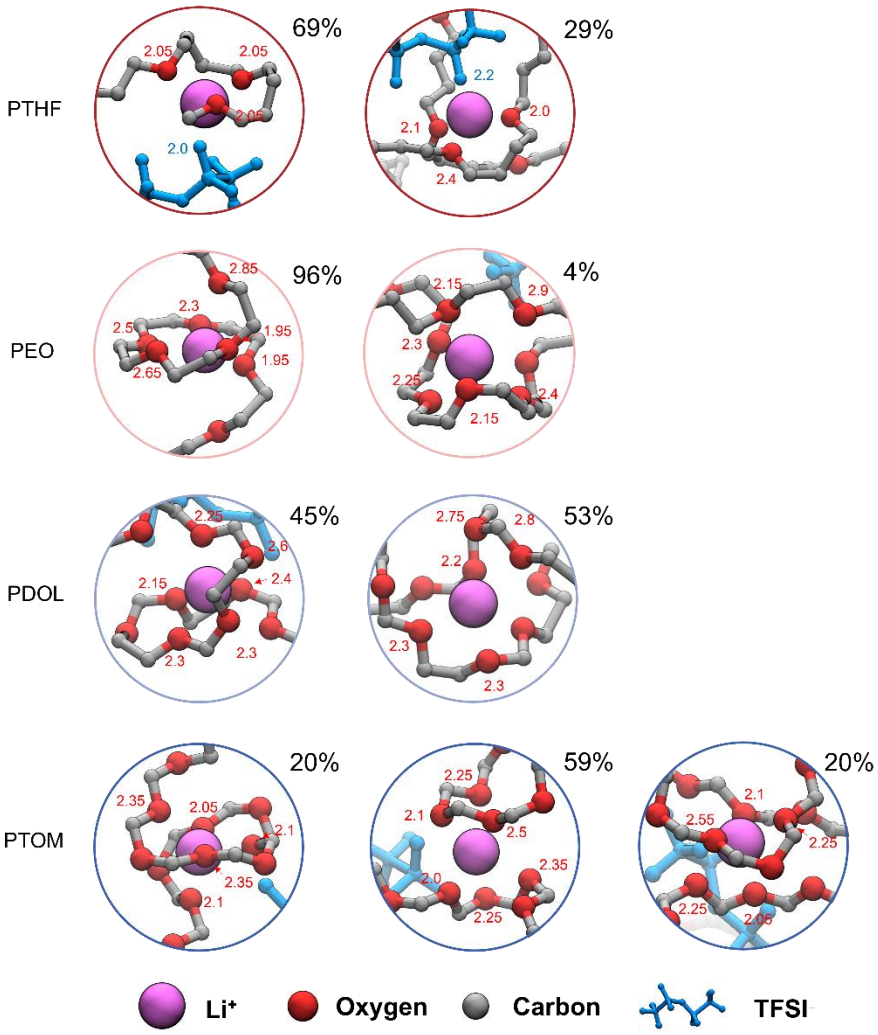

Fig. S25. Snapshots of representative solvation structures and their fractions in different systems. The first column is for one-chain binding, the second for two-chain, and the third for three-chain. The digitals indicate the distance of the first solvation shell oxygens to the Li^+. Hydrogen atoms are omitted for clarity.

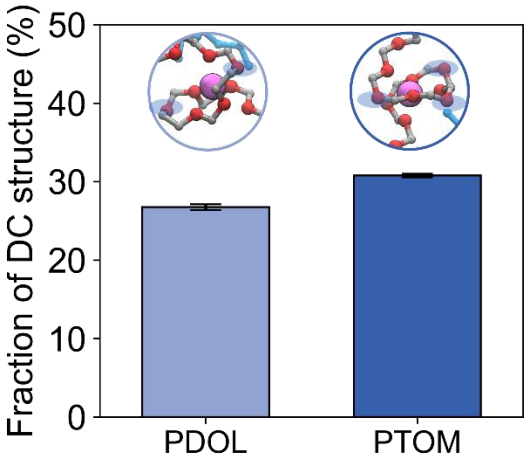

Fig. S26. The comparison of fractions of DC structure in PDOL and PTOM. The statistic structures include one-chain binding and multichain binding. Inset the one-chain binding structure for reference.

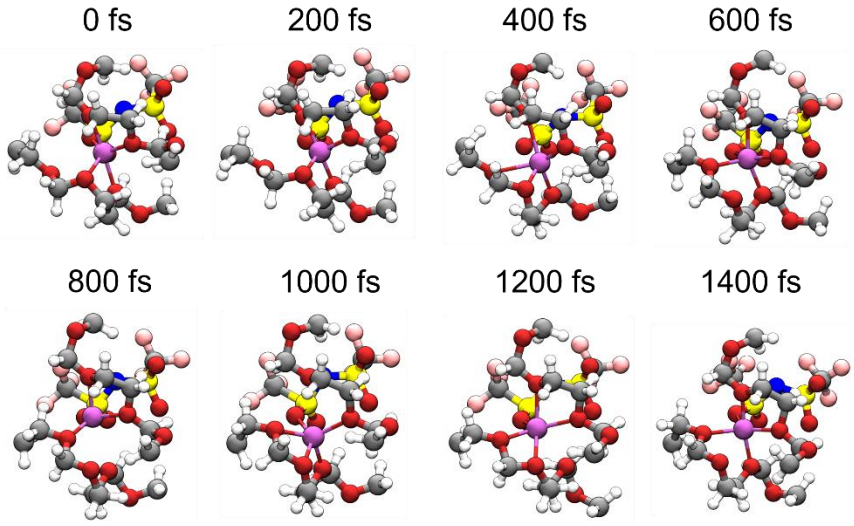

Fig. S27. Snapshots of PDOL solvation structures evolution in AIMD simulations. Discontinuous coordination structures are observed in 600 fs and 1400 fs.

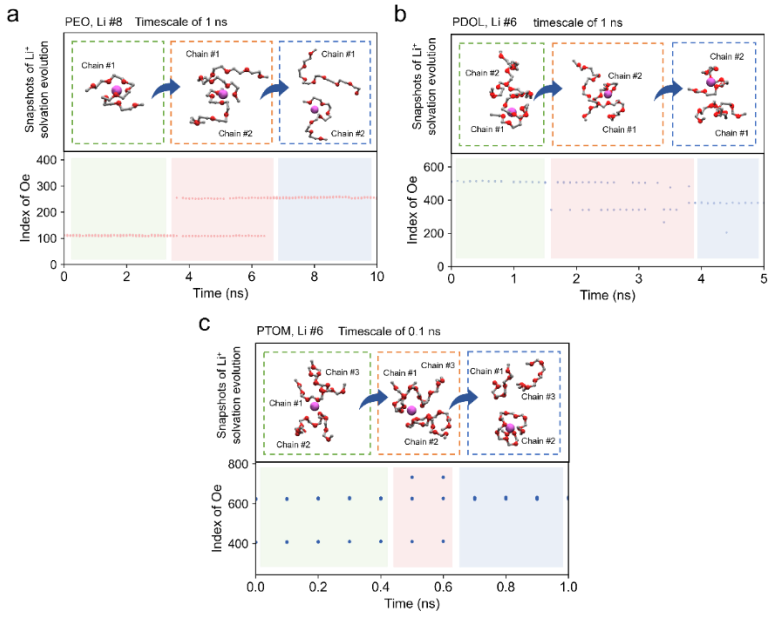

Fig. S28. Visualization of the interchain hopping dynamics process and the evolution of coordination of the tracked Li^+ for (a) PEO, (b) PDOL, and (c) PTOM. The interchain hopping events happen within distinct time scales, i.e., 1 ns for PEO and PDOL, and 0.1 ns for PTOM, respectively. Snapshots present the key steps of the interchain hopping process. Hydrogen atoms are omitted for clarity.

In PEO, Li^+ remains coordinated to chain #1, then binds simultaneously to chain #2 for approximately 2 ns before fully transferring, reflecting a slow, stepwise hopping process. In PDOL, a similar stepwise hopping transport is observed, while the event is more frequent due to its higher occurrence of two-chain binding. In contrast, Li^+ in PTOM engages in a dynamic three-chain coordination environment and completes interchain hopping within 0.2 ns, an order of magnitude faster.

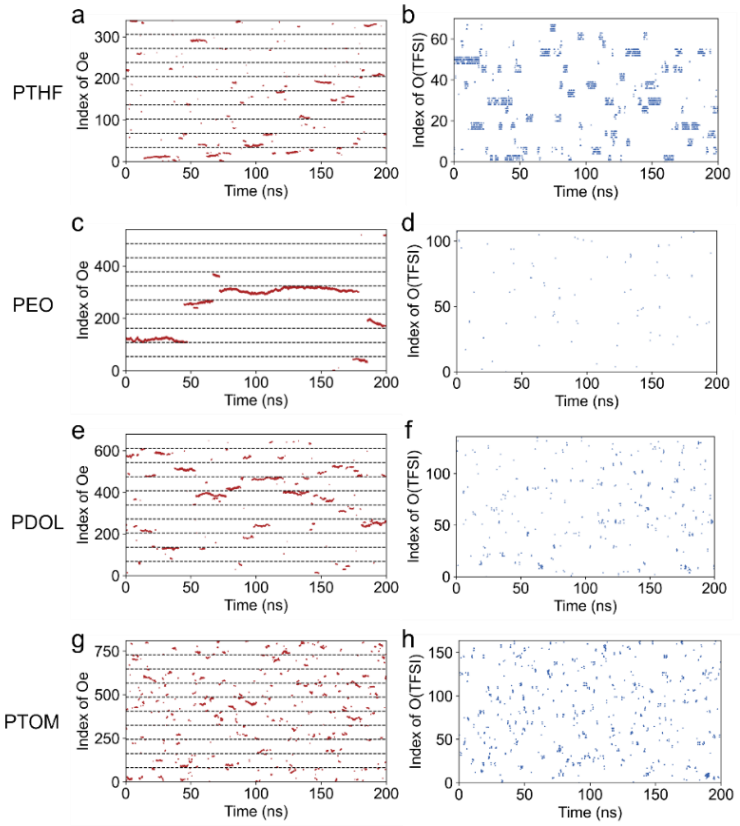

Fig. S29. Evolutions of the representative Li^+ coordination with Oe and $TFSI^-$ in different systems.

In PEO, Li^+ primarily exhibits one-chain coordination with minimal $TFSI^-$ interaction, and intrachain hopping predominates. In contrast, interchain hopping is more frequent in PTHF and PDOL, and most pronounced in PTOM. Additionally, the frequent Li^+–$TFSI^-$ coordination in PTHF reflects limited salt dissociation with a low Oe density. Overall, these findings attribute the enhanced Li^+ transport in PDOL and PTOM to their DC structures and prevalent multi-chain binding.

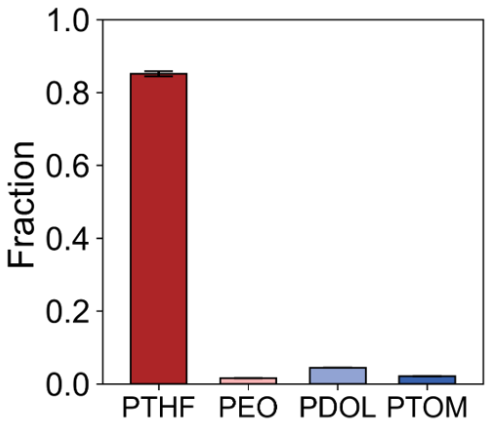

Fig. S30. The fraction of Li^+ with a coordination number less than or equal to four.

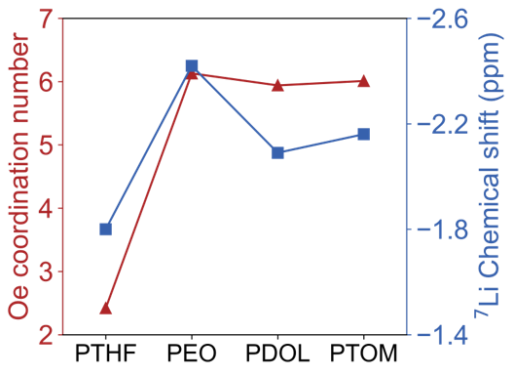

Fig. S31. Oe coordination numbers from MD simulations and ^{7}Li chemical shifts of the electrolytes.

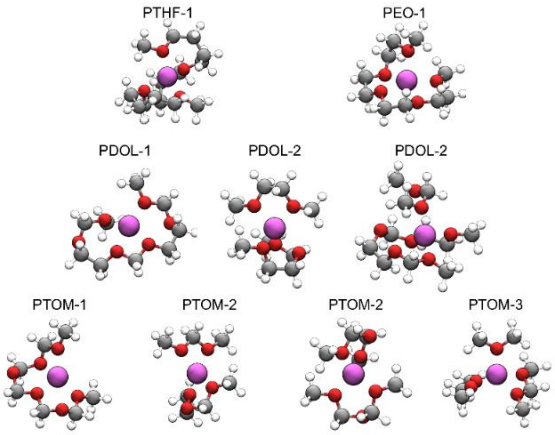

Fig. S32. Representative optimized Li^+–polymer complexes for binding free energy calculations, the number represents the binding chain number of Li^+.

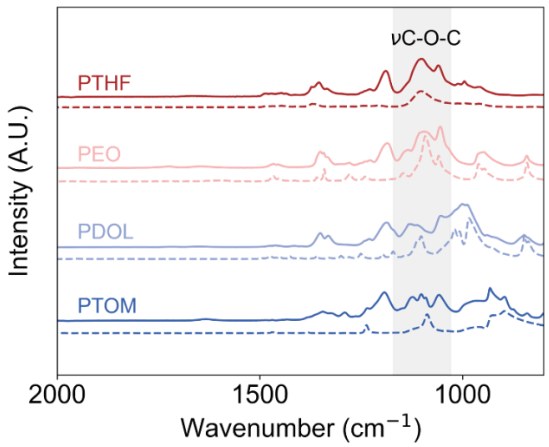

Fig. S33. ATR-FTIR spectra of the electrolytes (solid lines) and pure polymer (dashed lines).

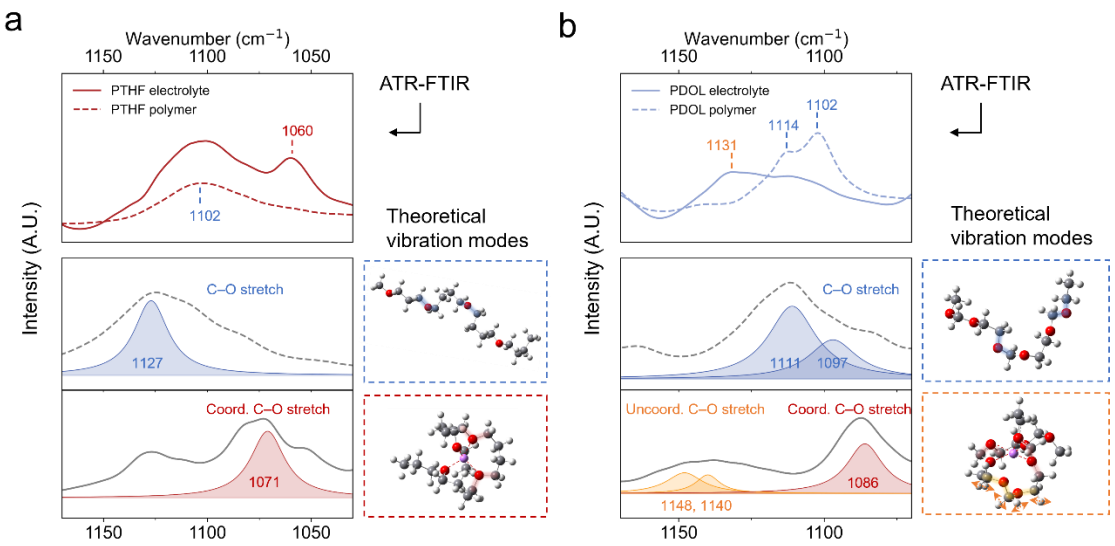

Fig. S34. The ATR-FTIR spectra of (a) PTHF electrolyte and PTHF polymer, as well as (b) PDOL electrolyte and PDOL polymer. The first row presents the experimental results, and the second and third rows display the theoretically calculated vibration modes and the corresponding structures.

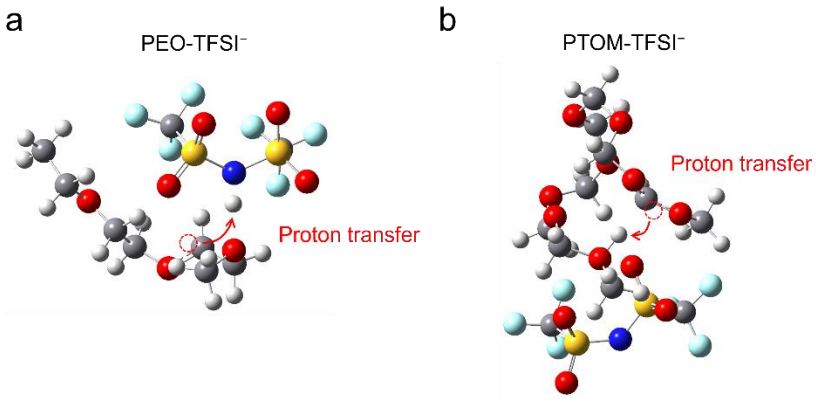

Fig. S35. Optimized structures at the oxidated states of (a) PEO-TFSI^{-1} complex and (b) PTOM-TFSI^{-1} complex where proton transfers are observed.

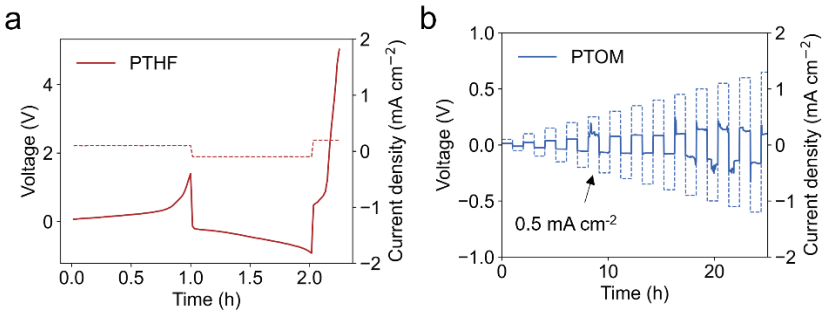

Fig. S36. The CCD tests of Li/polymer electrolyte/Li symmetric cells for (a) PTHF and (b) PTOM.

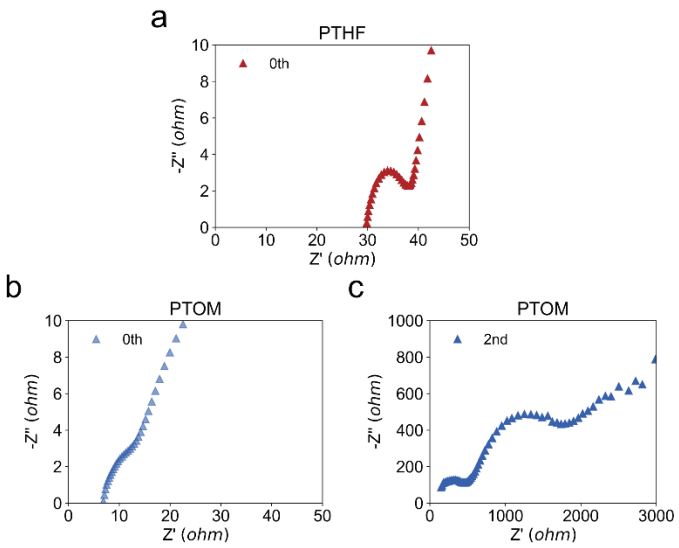

Fig. S37. Electrochemical impedance spectra (EIS) profiles. (a) The Li/PTHF/LFP cells at the 0^{th} cycle. The Li/PTOM/LFP cell at (b) the 0^{th} cycle and (c) the 2^{nd} cycle. The Li/PTHF/LFP cell exhibits large internal impedance at the 0^{th} cycle. The Li/PTOM/LFP presents increased impedance at the 2^{nd} cycle.

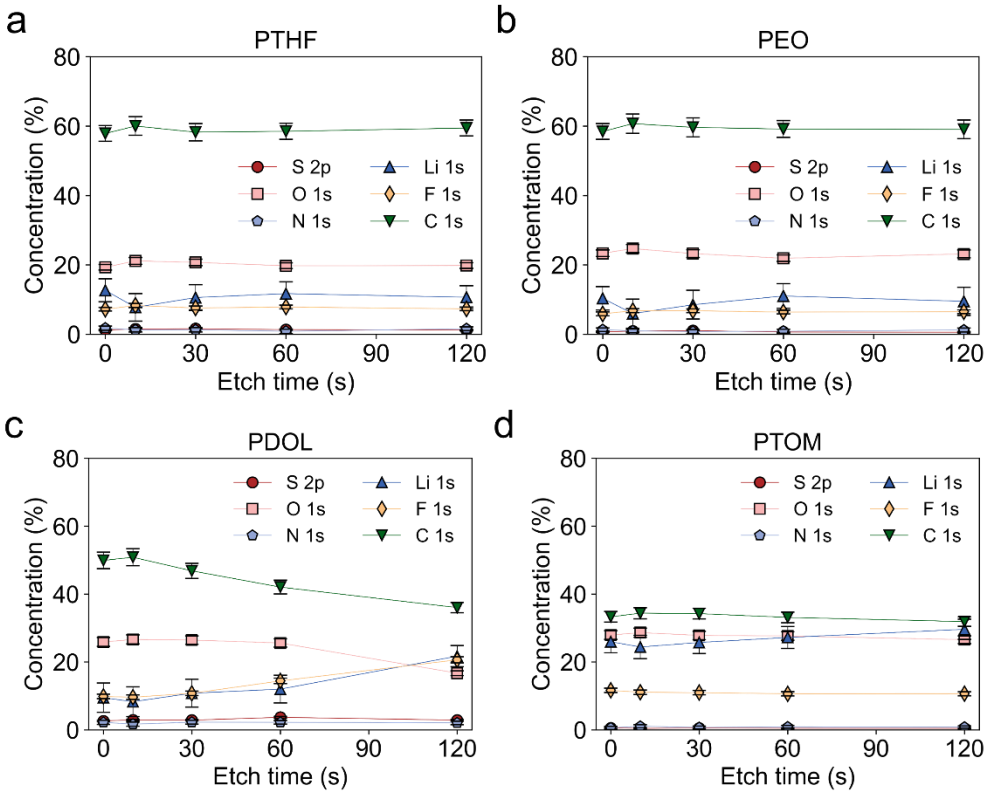

Fig. S38. X-ray photoelectron spectroscopy (XPS) derived composition depth profile versus etch time for (a) PTHF, (b) PEO, (c) PDOL, and (d) PTOM.

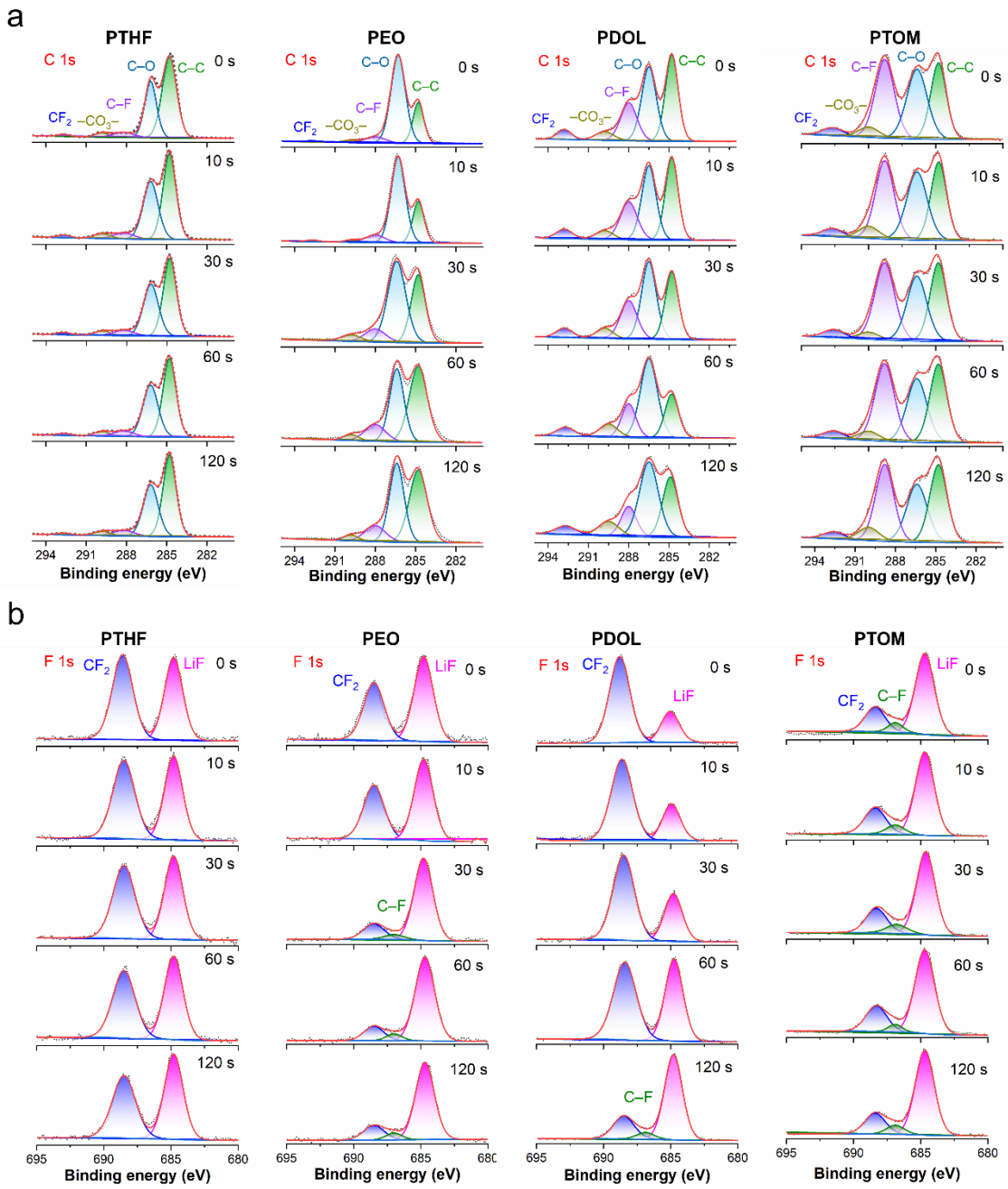

Fig. S39. The (a) C 1s and (b) F 1s XPS depth profiles of the solid-electrolyte interphases.

Table S1. Compositions of the MD simulation box for different electrolyte systems.

System	Structure of repeat unit [a]	Degree of polymerization	Chain number	Salt number	Li:Oe
PTHF	-$CH_2CH_2CH_2CH_2O$-	34	10	17	1:20
PEO	-CH_2CH_2O-	54	10	27	1:20
PDOL	-$CH_2CH_2OCH_2O$-	34	10	34	1:20
PTOM	-CH_2O-	81	10	41	1:20

[a] All polymer chains are terminated by -CH_3 group.

Table S2. Systems setup for convergence test.

Chain numbers	Degree of polymerization	Salt number	Li:Oe	Box length (Å)
5	52	13	1:20	28.11 ± 0.12
8	50	20	1:20	32.45 ± 0.11
10	54	27	1:20	35.82 ± 0.19
20	54	54	1:20	45.11 ± 0.03

Table S3. Compositions of the AIMD simulation box.

System	Polymer structure formula	Chain number	Salt number
PTHF	$CH_3(CH_2CH_2CH_2CH_2O)_5CH_3$	8	2
PEO	$CH_3(CH_2CH_2O)_{10}CH_3$	6	3
PDOL	$CH_3(CH_2CH_2OCH_2O)_5CH_3$	6	3
PTOM	$CH_3(CH_2O)_{10}CH_3$	6	3

Table S4. Compositions of the MD simulation box for different concentrations.

System	Structure of repeat unit [a]	Degree of polymerization	Chain number	Salt number	Li:Oe
PTHF	-$CH_2CH_2CH_2CH_2O$-	34	10	17	1:20
PEO	-CH_2CH_2O-	54	10	27	1:20
PDOL	-$CH_2CH_2OCH_2O$-	34	10	34	1:20
PTOM	-CH_2O-	81	10	41	1:20
PTHF	-$CH_2CH_2CH_2CH_2O$-	34	10	34	1:10
PEO	-CH_2CH_2O-	54	10	54	1:10
PDOL	-$CH_2CH_2OCH_2O$-	34	10	68	1:10
PTOM	-CH_2O-	81	10	82	1:10
PTHF	-$CH_2CH_2CH_2CH_2O$-	34	10	26	1:7.5
PEO	-CH_2CH_2O-	54	10	72	1:7.5
PDOL	-$CH_2CH_2OCH_2O$-	34	10	91	1:7.5
PTOM	-CH_2O-	81	10	108	1:7.5

[a] All polymer chains are terminated by -CH_3 group.

Table S5. Comparison of calculated $\boldsymbol{\tau_1}$, mean squared chemical bond length $\boldsymbol{b_0^2}$, mean squared end-to-end distance $\boldsymbol{\langle R_e^2 \rangle}$, $\boldsymbol{\tau_R}$, $\boldsymbol{\tau_2}$, and $\boldsymbol{\tau_3}$ for the PEO system. [a]

	τ_1	b_0^2 [Å^2]	$\langle R_e^2 \rangle$ [Å^2]	τ_R	τ_2	τ_3
Reference [19]	147	9.7	1573 ± 112	45	167	17.1 ± 1.3
This work	126.7 ± 7.5	8.8 ± 0.3	1366 ± 64	54.1 ± 14.9	128.5 ± 34.1	13.5 ± 0.6

[a] The results of this work displayed in this table were obtained using the same criteria in reference [19].

Table S6. The molecular polarity index (MPI) and fraction of polar surface area.[a]

	PTHF	PEO	PDOL	PTOM
MPI (eV)	0.25	0.36	0.49	0.60
Fraction of polar surface area (%)	12.68	21.31	38.31	55.83

[a] Typically, a higher MPI and fraction of polar surface area indicate higher local polarity.

References

1. C. Klein, J. Sallai, T. J. Jones, C. R. Iacovella, C. McCabe and P. T. Cummings, in *Foundations of Molecular Modeling and Simulation: Select Papers from FOMMS 2015*, eds. R. Q. Snurr, C. S. Adjiman and D. A. Kofke, Springer Singapore, Singapore, 2016.
2. C. Klein, A. Z. Summers, M. W. Thompson, J. B. Gilmer, C. McCabe, P. T. Cummings, J. Sallai and C. R. Iacovella, *Comput. Mater. Sci.*, 2019, **167**, 215–227.
3. A. I. Jewett, D. Stelter, J. Lambert, S. M. Saladi, O. M. Roscioni, M. Ricci, L. Autin, M. Maritan, S. M. Bashusqeh, T. Keyes, R. T. Dame, J.-E. Shea, G. J. Jensen and D. S. Goodsell, *J. Mol. Biol.*, 2021, **433**, 166841.
4. R. H. Byrd, P. Lu, J. Nocedal and C. Zhu, *SIAM J. Sci. Comput.*, 1995, **16**, 1190–1208.
5. G. Bussi, D. Donadio and M. Parrinello, *J. Chem. Phys.*, 2007, **126**.
6. S. Mogurampelly, J. R. Keith and V. Ganesan, *J. Am. Chem. Soc.*, 2017, **139**, 9511–9514.
7. R. J. Gowers and P. Carbone, *J. Chem. Phys.*, 2015, **142**, 224907.
8. K. D. Fong, H. K. Bergstrom, B. D. McCloskey and K. K. Mandadapu, *AIChE J.*, 2020, **66**, e17091.
9. J. Self, K. D. Fong and K. A. Persson, *ACS Energy Lett.*, 2019, **4**, 2843–2849.
10. T. Hou, K. D. Fong, J. Wang and K. A. Persson, *Chem. Sci.*, 2021, **12**, 14740–14751.
11. Y. Shao, H. Gudla, D. Brandell and C. Zhang, *J. Am. Chem. Soc.*, 2022, **144**, 7583–7587.
12. K. D. Fong, J. Self, B. D. McCloskey and K. A. Persson, *Macromolecules*, 2020, **53**, 9503–9512.
13. K. D. Fong, J. Self, K. M. Diederichsen, B. M. Wood, B. D. McCloskey and K. A. Persson, *ACS Cent. Sci.*, 2019, **5**, 1250–1260.
14. J. Han, R. H. Gee and R. H. Boyd, *Macromolecules*, 2002, **27**, 7781–7784.
15. H. Gudla and C. Zhang, *J. Phys. Chem. B*, 2024, **128**, 10537–10540.
16. A. Hagberg, P. Swart and D. S Chult, *Exploring network structure, dynamics, and function using NetworkX*, Los Alamos National Lab.(LANL), Los Alamos, NM (United States), 2008.
17. A. Maitra and A. Heuer, *Phys. Rev. Lett.*, 2007, **98**, 227802.
18. D. Diddens, A. Heuer and O. Borodin, *Macromolecules*, 2010, **43**, 2028–2036.
19. D. Diddens and A. Heuer, *J. Phys. Chem. B*, 2014, **118**, 1113–1125.